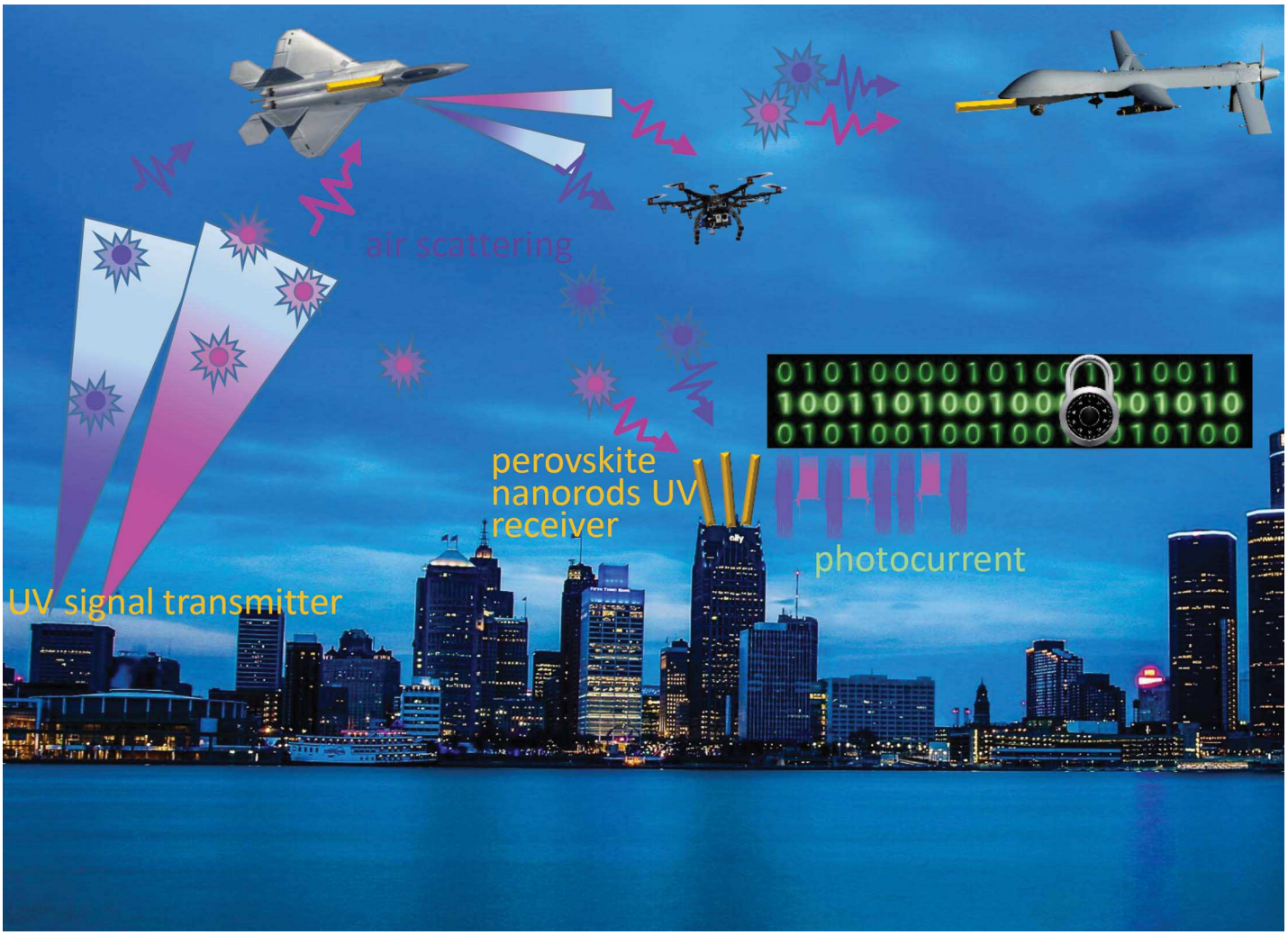

The cover artwork showcases a study on wavelength-distinguishable UV detection via bipolar photoelectron injections in lithium chloride-promoted formamidinium lead trichloride perovskite nanorods, as led by Prof. Tao Xu from Northern Illinois University.

Energy-distinguishable bipolar UV photoelectron injection from LiCl-promoted $FAPbCl_3$ perovskite nanorods

Photodetectors that can unambiguously distinguish UV photons of different wavelengths are exceptionally desirable for high-speed, cyber-secured, wide-coverage and non-line-of-sight UV communications. This study reveals that LiCl-promoted solution-grown $FAPbCl_3$ perovskite nanorods exhibit novel distinguishability towards 365 nm and 254 nm UV photons through perturbed photocurrent polarities, making them very promising for decoding the information enciphered in UV photons with different energies, thus providing an alternative way towards high-performance UV-based information science and communication.

As featured in:

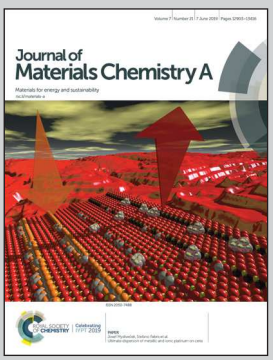

See Tao Xu *et al.*, *J. Mater. Chem. A*, 2019, **7**, 13043.

ROYAL SOCIETY OF CHEMISTRY | Celebrating IYPT 2019

rsc.li/materials-a

Registered charity number: 207890

Journal of Materials Chemistry A

PAPER

View Article Online
View Journal | View Issue

Cite this: J. Mater. Chem. A, 2019, 7, 13043

Energy-distinguishable bipolar UV photoelectron injection from LiCl-promoted $FAPbCl_3$ perovskite nanorods†

Jue Gong,[a] Xun Li,[a] Peijun Guo,[b] Ian Zhang,[a] Wei Huang,[cd] Ke Lu,[a] Yingwen Cheng,[a] Richard D. Schaller,[bc] Tobin J. Marks[cd] and Tao Xu*[a]

Received 30th January 2019
Accepted 4th April 2019

DOI: 10.1039/c9ta01160a

rsc.li/materials-a

High-performance optoelectronic devices, such as solar cells and light-emitting diodes, have been fabricated with lead halide perovskites owing to their superior carrier properties. However, charge transport in such optoelectronics is intrinsically directional due to the existence of p–n junctions, which thus lacks the potential to elucidate any perturbations in light or electricity during energy conversion. Here, with the presence of a LiCl additive in a formamidinium chloride (FACl) solution, the as-grown LiCl:$FAPbCl_3$ nanorods demonstrate greatly enhanced crystallinity and UV photoresponse as compared to pristine $FAPbCl_3$ nanostructures without the LiCl additive. Most importantly, the LiCl:$FAPbCl_3$ nanorod film exhibits unprecedented distinguishability to UV photons with different energies and oscillating intensities, in the form of bipolar and periodically oscillatory photocurrents. This work could advance the fundamental understanding of photoinduced carrier processes in halide perovskites and facilitate the development of novel UV-based optical communications.

Introduction

Ultraviolet (UV) radiation has given rise to high-speed, wide-coverage and non-line-of-sight wireless optical communications due to its small susceptibility to solar background interference and flexibility of transmitter/receiver orientations such as pointing, acquisition and tracking.[1–4] For a wireless UV communication, a function generator produces pattern-controlled electrical signals that contain characteristic information on the intensity and on–off frequency of UV photons, which are emitted by a transmitter and subsequently detected by a receiver to realize the relay of information.[2,5] Moreover, UV radiation with different wavelengths is employed in communication systems so as to enable bidirectional and high-capacity optical transmission, where a large distinction between UV wavelengths is demanded for minimized inter-channel interference.[2,6] Therefore, developing a photodetector that can accurately identify UV intensity variation, while simultaneously distinguishing UV photons having different wavelengths, is highly desirable for acquiring and decoding the information embedded in UV carriers. Owing to their suitable bandgaps and superior charge transport properties, lead halide perovskites (*e.g.* $MAPbCl_3$, $CsPbCl_3$, and $FAPbI_3$) have been used to realize high-performance UV photodetectors.[7–14] Nonetheless, such photodetectors were never able to differentiate UV photons with different energies due to the indiscriminate, unidirectional transport of photogenerated charge carriers in (1) prototypical p–i–n photodiode structures,[7,8] (2) lateral photoconductor structures with external voltage biases,[9,12–14] and (3) devices utilizing metal electrodes with highly discrepant work functions for guided carrier migration.[10] In addition, photodetectors need to be sufficiently sensitive to accurately detect UV photons with temporally varying intensities based on superior photoelectronic properties (*e.g.* large free carrier density and high mobility), since optical information can also be ciphered in the oscillating intensities. As such, it is intriguing both at scientific and technological levels to develop a UV photodetector that permits multidirectional carrier transport in perovskite materials with radically improved optoelectronic properties, so as to observe perturbed photocurrent responses and to eventually elucidate the energies and intensities of UV photons. Herein, through the lithium chloride (LiCl, 1 mg mL^{-1}) additive mixed in formamidinium chloride (FACl, 10 mg mL^{-1})/isopropanol solution, the synthesized formamidinium lead chloride ($FAPbCl_3$) nanorods (detailed methods elaborated in the ESI†) exhibit significantly improved crystallinity and enhanced photoresponse upon 365 nm UV illumination (powered by direct current (DC)), in comparison with the pristine $FAPbCl_3$

[a]Department of Chemistry and Biochemistry, Northern Illinois University, DeKalb, IL 60115, USA. E-mail: txu@niu.edu

[b]Center for Nanoscale Materials, Argonne National Laboratory, Argonne, IL 60439, USA

[c]Department of Chemistry, Northwestern University, 2145 Sheridan Road, Evanston, IL 60208, USA

[d]Materials Research Center, Northwestern University, 2145 Sheridan Road, Evanston, IL 60208, USA

† Electronic supplementary information (ESI) available. See DOI: 10.1039/c9ta01160a

nanostructures grown without the LiCl additive. In this way, the high-crystallinity LiCl-promoted $FAPbCl_3$ (LiCl:$FAPbCl_3$) nanorod films display sensitive distinguishability between alternating current (AC) powered 254 nm and AC powered 365 nm UV illuminations with oscillatory light intensities *via* periodically damping and bipolar photocurrents.

Results and discussion

X-ray diffraction (XRD) was first performed to characterize the structural properties of the as-synthesized LiCl:$FAPbCl_3$ and $FAPbCl_3$ nanostructures. As shown in Fig. 1a, the solution-grown LiCl:$FAPbCl_3$ nanostructured film (red trace) displays diffraction peaks of the (100), (110) and (200) planes with much greater intensities in contrast with its $FAPbCl_3$ counterpart (blue trace). Quantitatively, the large peak intensity ratios, ~5.4, ~2.9, ~7.6 for (100), (110), (200) planes respectively, prove the greater crystallinity of LiCl:$FAPbCl_3$ relative to $FAPbCl_3$. Also, the preferred crystallographic orientations of LiCl:$FAPbCl_3$ are notably changed relative to pristine $FAPbCl_3$, which agrees well with the fact that additives/dopants can effectively alter materials' microstructures.[16–18] The XRD patterns of both perovskite $FAPbCl_3$ films closely match the reported pattern (black),[15] and therefore indicate complete reaction of the $PbCl_2$ (green) and LiCl (magenta) precursors. Structural refinement of the LiCl:$FAPbCl_3$ film reveals an enlarged cell parameter (~5.8505 Å) in contrast to the reported 5.7379 Å, thereby indicating the doping of Li^+ in the material lattice, as shown in Fig. S1.† X-ray photoelectron spectroscopy (XPS) unambiguously confirms the presence of Li^+ within the LiCl:$FAPbCl_3$ nanorods, along with the constituent C, N, Pb and Cl elements, as shown in Fig. S2.† From the XPS study, the Pb to Li atomic ratio is calculated to be ~1.6 (Table S2†).

Detailed analysis of the diffraction peaks reveals notably smaller FWHMs on the LiCl:$FAPbCl_3$ film (Fig. 1b), thereby signifying much larger crystalline domains[19] of $FAPbCl_3$ nanostructures grown with the LiCl additive than the pristine $FAPbCl_3$ counterpart, as verified on (200), (110) and (100) orientations (Fig. 1c) through Scherrer's equation—$D = k\lambda/b\cos\theta$,[20–22] in which D, k, λ, b and θ respectively represent the crystallite size, shape factor (0.9), wavelength of X-ray photons (1.54 Å for Cu Kα radiation), FWHM and diffraction angle. Additionally, LiCl:$FAPbCl_3$ clearly exhibits fluorescence with a redshifted peak intensity at 432 nm (Fig. 1d) with respect to pristine $FAPbCl_3$ at 420 nm. The distinctively narrowed optical bandgap has once again corroborated enhanced crystallinity in perovskite materials.[23–25] Also, the FWHM of the LiCl:$FAPbCl_3$ fluorescence peak (~53 nm) is smaller than that of pristine $FAPbCl_3$ (~57 nm), which implies a more homogeneous band structure for LiCl:$FAPbCl_3$ due to the crystallinity improvement. Explicitly, LiCl:$FAPbCl_3$ nanowires display a highly ordered morphology featuring sharp edges and flat end facets on micrometre-size crystals, in contrast to pristine $FAPbCl_3$ nanostructures that are much more disordered in shape, as

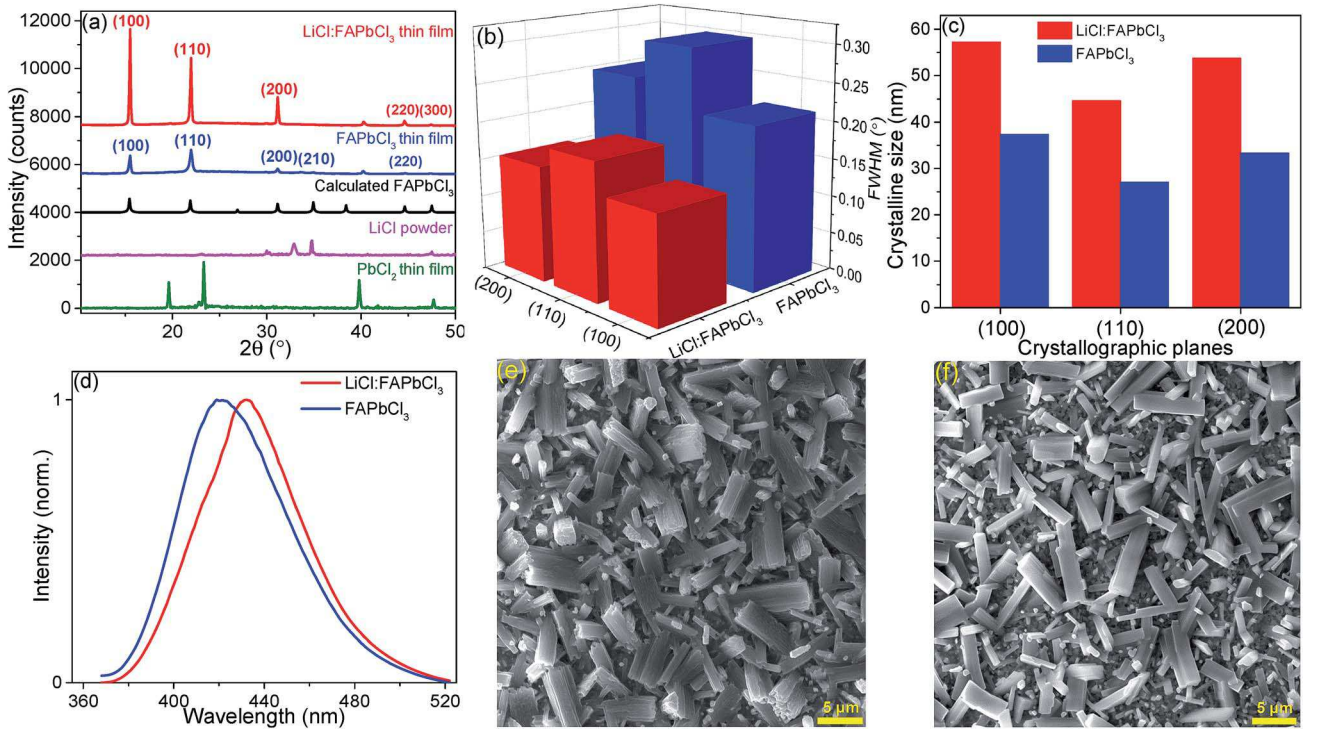

Fig. 1 Crystallinity analysis of pristine $FAPbCl_3$ and LiCl:$FAPbCl_3$ nanostructured films. (a) XRD patterns of $FAPbCl_3$ nanostructures grown with the LiCl additive (red), without the LiCl additive (blue), reported $FAPbCl_3$ (black) by Govinda *et al.*,[15] and $PbCl_2$ (green) and LiCl (magenta) precursors. (b) FWHMs of pristine $FAPbCl_3$ (blue) and LiCl:$FAPbCl_3$ (red). (c) Summary of crystallite sizes for (100), (110) and (200) crystallographic planes. (d) Fluorescence spectra of LiCl:$FAPbCl_3$ (red) and pristine $FAPbCl_3$ (blue). SEM images of pristine $FAPbCl_3$ (e) and LiCl:$FAPbCl_3$ (f) nanostructures under 5.21k× magnification.

shown in Fig. 1e and f. From the chemistry perspectives, the higher crystallinity of LiCl:$FAPbCl_3$ nanorods stems from the dissolution and recrystallization process (Ostwald ripening)[26–29] caused by the large concentration of Cl^- from the LiCl additive (see the ESI Methods section for details†). This claim can be validated by $FAPbCl_3$ that is grown from a high-concentration FACl precursor (~12 mg mL^{-1}, contains an equivalent amount of Cl^- as in LiCl:$FAPbCl_3$), which also exhibits significantly stronger (100) and (200) reflections (Fig. S3†) than $FAPbCl_3$ with a 10 mg mL^{-1} FACl precursor (Fig. 1a blue) and thus signifies its much higher crystallinity. Furthermore, addition of Li^+ selectively helps to improve the crystallinity of the resulting $FAPbCl_3$ nanorods as seen in the (110) reflection, as compared with the greatly suppressed (110) plane in high-concentration FACl-promoted $FAPbCl_3$ (Fig. S3†), agreeing well with K^+ doping reported previously.[30,31] To validate the feasibility of a UV photodetector, optical reflectance was subsequently performed on the pristine $FAPbCl_3$ nanostructured films, where the amount of light reflected quickly falls as the photon wavelength goes below 400 nm (Fig. S4†), thereby indicating the large absorption of UV photons and the consequent generation of photoelectrons. Indeed, as shown in Fig. 2a, upon on–off switching of 365 nm UV illumination, both pristine $FAPbCl_3$ and LiCl:$FAPbCl_3$ photodetectors (fabrication methods elaborated in the ESI†) show a functional photocurrent response. Nevertheless, the LiCl:$FAPbCl_3$ film exhibits remarkably larger photocurrent densities at around 9 μA cm^{-2} in contrast with 1.6 μA cm^{-2} for pristine $FAPbCl_3$, which represents more than a 5-fold increase and therefore demonstrates greatly enhanced optoelectronic performance due to LiCl-induced crystallinity improvement. Detailed studies of the rise and decay behaviours of single on–off current cycles show much faster rising kinetics for the LiCl:$FAPbCl_3$ photodetector over the $FAPbCl_3$ counterpart, as shown in Fig. S5,† and thus signifies a greater photoelectric sensitivity on the LiCl:$FAPbCl_3$ photodetector. Comparatively, as shown in Table S2,† responsivities of LiCl:$FAPbCl_3$ (~167 mA W^{-1}) and $FAPbCl_3$ (~29 mA W^{-1}) photodetectors are notably greater than that of devices based on ZnO thin films (0.1 mA W^{-1}),[32] $LiNbO_3$ single crystals (17.1 mA W^{-1}),[33] $LiTaO_3$ single crystals (2 mA W^{-1})[34] and $LaAlO_3$ single crystals (71.8 mA W^{-1}).[35] It thus indicates the promising suitability of LiCl:$FAPbCl_3$ and $FAPbCl_3$ in UV detection. Synergistically, the improved crystallinity on LiCl:$FAPbCl_3$ also leads to outstandingly enhanced photostability, in which LiCl:$FAPbCl_3$ retained ~80% of its original photocurrent density after 900 seconds of continuous UV illumination while pristine $FAPbCl_3$ exhibited <60% retention of its initial current density, as shown in Fig. 2b. Accordingly, what accounts for the enhanced photoelectric performance of the LiCl:$FAPbCl_3$ nanostructured films are their notably improved charge transport kinetics. It is unambiguous to see that LiCl:$FAPbCl_3$ has exceptionally increased electrical conductivity (Fig. 2c) and much smaller electrochemical impedance (Fig. 2d) as compared to the pristine $FAPbCl_3$ counterpart. By adopting a common

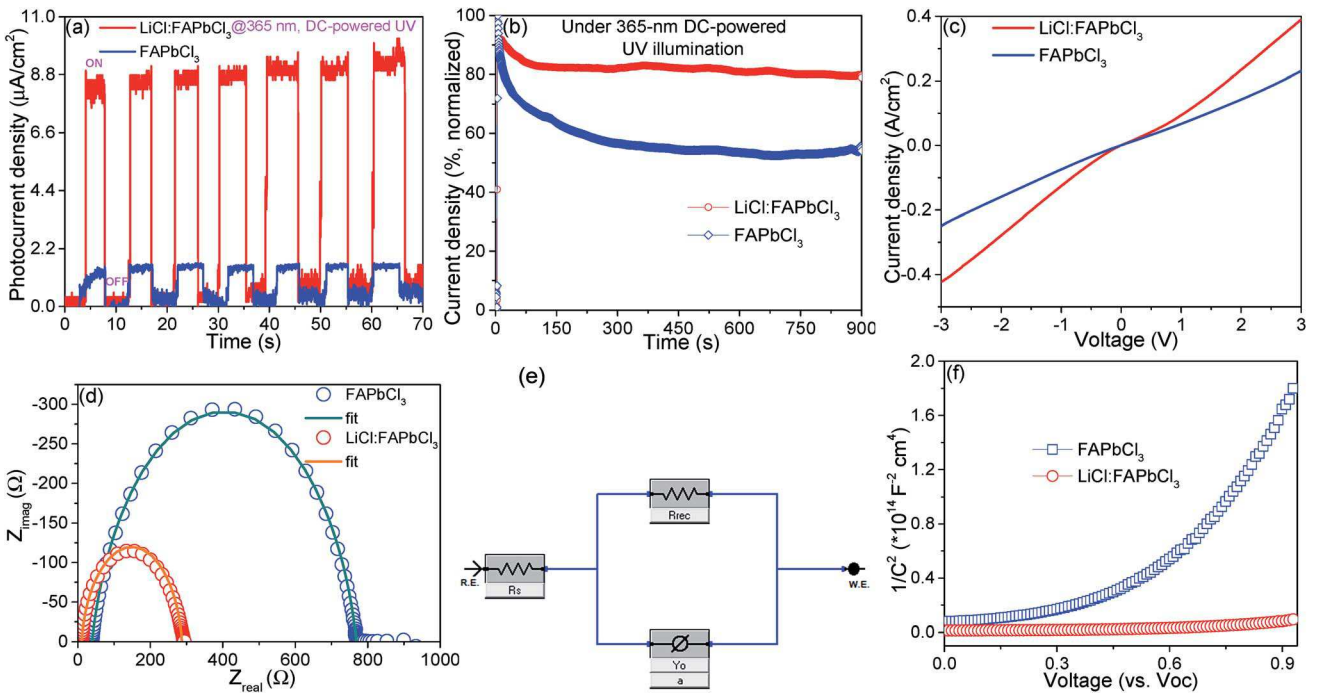

Fig. 2 UV photoresponse and electrical characteristics of LiCl:$FAPbCl_3$ (red) and pristine $FAPbCl_3$ (blue) nanostructured films. On–off photocurrents of LiCl:$FAPbCl_3$-based (red) and $FAPbCl_3$-based (blue) photodetectors under DC-powered 365 nm UV illumination (a), photostability plots of pristine $FAPbCl_3$ (blue) and LiCl:$FAPbCl_3$ (red) nanostructured films under continuous illumination of DC-powered 365 nm UV light (b). Dark currents were subtracted to align the baselines of LiCl:$FAPbCl_3$ and $FAPbCl_3$ photodetectors in (a). (c) Linear sweep voltammogram of the perovskite films measured under dark conditions. (d) Nyquist plots of the perovskite films under DC-powered 365 nm UV illumination. (e) Equivalent circuit applied in fitting the impedance curves shown in (d). (f) Mott–Schottky plots of the perovskite films measured under DC-powered 365 nm UV illumination.

Table 1 Summary of R_{rec}, CPE and time constants obtained from the electrochemical impedance fittings in Fig. 2d

Perovskite film	R_{rec} (Ω)	CPE (F)	Lifetime (s)
$FAPbCl_3$	729.6	1.97×10^{-6}	0.00144
LiCl:$FAPbCl_3$	276.9	5.41×10^{-7}	0.000150

resistance//capacitance ($R//C$) circuit model for metal/perovskite/metal constructions[36,37] as shown in Fig. 2e, the charge recombination resistances (R_{rec}), chemical capacitances (constant phase element, CPE) and the electron transit times ($R_{rec} \times$ CPE) were calculated and are summarized in Table 1. The fact that LiCl:$FAPbCl_3$ exhibited a shorter electron lifetime (0.000150 s) than pristine $FAPbCl_3$ (0.00144 s) implies its exceptionally greater carrier mobility.[38]

As shown in Fig. 2f, Mott–Schottky plots further suggest that LiCl:$FAPbCl_3$ has remarkably greater free carrier density (1.98×10^{17} cm^{-3}) in contrast to pristine $FAPbCl_3$ (1.03×10^{16} cm^{-3}), as evidenced by its much smaller voltage-dependent slope through the following equation:[39,40]

$$N_c = \frac{2}{e_0 \varepsilon \varepsilon_0} \left[\frac{\partial \left(\frac{1}{C^2} \right)}{\partial V} \right]^{-1}$$

where N_c, e_0, ε, ε_0 and $[\partial(1/C^2)/\partial V]$ stand for the carrier concentration, electron charge (1.602×10^{-19} C), dielectric constant ($\approx$30 for pristine $FAPbCl_3$ at room temperature),[15] vacuum permittivity (8.854×10^{-12} F m^{-1}) and slope of the Mott–Schottky plot, respectively.

Importantly, the abovementioned photoresponse was achieved with a UV light source powered by batteries (UVL-4F UV lamp, picture shown in Fig. S6†), which therefore was operated at constant current and UV light intensity. This is verified by Fourier transform (FT) of LiCl:$FAPbCl_3$ on–off photocurrents (Fig. S7†), where no frequency components are found and therefore signifies the absence of periodically oscillating photocurrents. Nevertheless, in the presence of AC-powered 60 Hz 365 nm UV illumination (UVGL-25, picture shown in Fig. S8†), LiCl:$FAPbCl_3$ exhibited photocurrents with oscillating magnitudes (Fig. 3a–c), which is on par with the oscillatory nature of UV light intensity and implies a highly sensitive photoelectronic response of the LiCl:$FAPbCl_3$-based device. Moreover, by performing FT of the observed chronoamperogram, distinctive frequency components—60 Hz, 120 Hz, 180 Hz and 240 Hz—are detected, as shown in Fig. S9,† which thus indicate that photocurrents are periodically oscillating and closely echo the 60 Hz current oscillation frequency of the 365 nm UV light source (Fig. S8†). Astonishingly, under 254 nm AC-powered UV illumination, the LiCl:$FAPbCl_3$ detector unexpectedly shows current signals both above and below the dark current, and hence suggests that the UV-induced photoelectron injection is periodically switching directions, as shown in Fig. 3d–f.

The periodically damping nature of 60 Hz 254 nm photocurrents is once again confirmed by the FT coefficient plot of the observed chronoamperogram. Similarly, frequency-domain

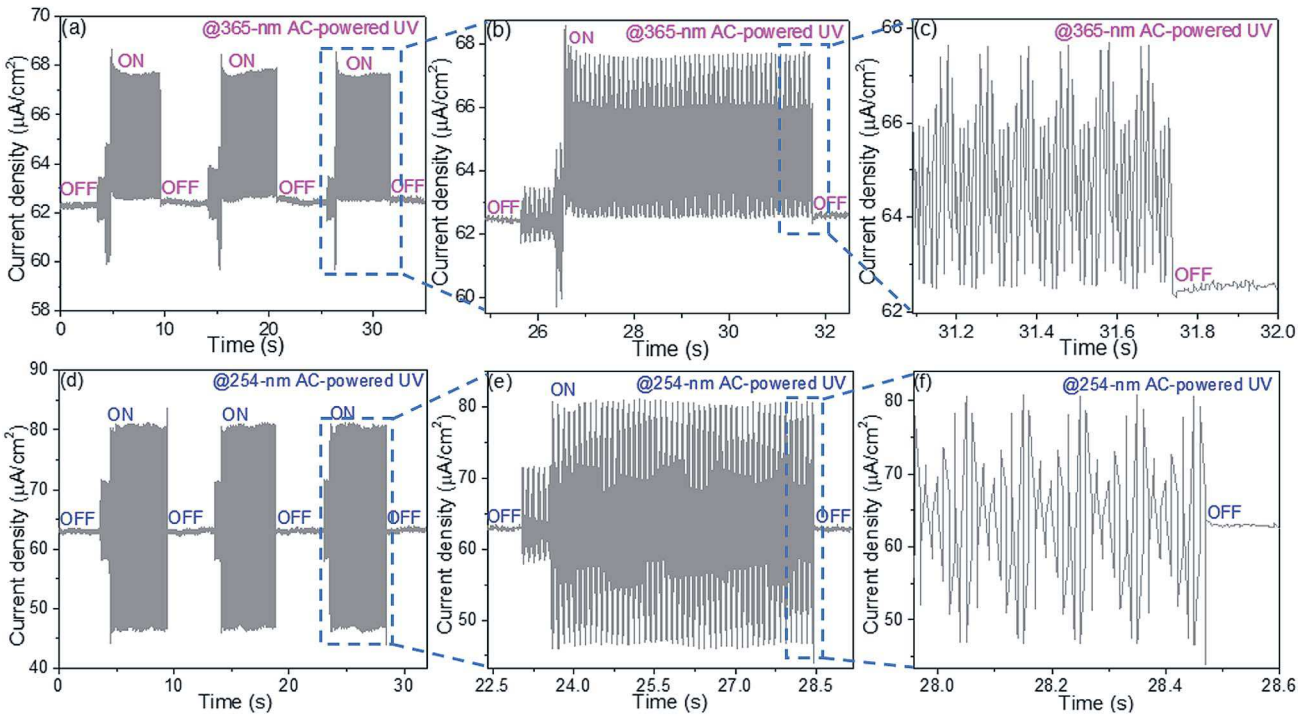

Fig. 3 Time-dependent UV photoresponse of the perovskite photodetectors. On–off photocurrents of the LiCl:$FAPbCl_3$-based photodetector under 365 nm AC-powered UV illumination (a) and 254 nm AC-powered UV illumination (d), and zoomed-in views of the 365 nm UV photocurrent signals (b, c) and 254 nm photocurrent signals (e, f).

coefficient plots clearly show the existence of a 60 Hz frequency component, which is characteristic of 120 Hz, 180 Hz and 240 Hz harmonic current frequencies (Fig. 4) and again closely corroborates the 60 Hz current/light intensity oscillation frequency (Fig. S8†). Finally, by quantitatively analyzing the FT coefficient plots of the 60 Hz 365 nm/254 nm photocurrents (Fig. S9† and 4), one can find that the magnitudes of the coefficients under 254 nm UV are much greater than the 365 nm counterparts. Moreover, 365 nm-induced photocurrents have a frequency distribution between 100 and 150 Hz that is comparable with the frequency distributions in the ranges of 50–75 Hz and 175–200 Hz. This frequency profile, however, is evidently different from 254 nm FT coefficients, which have very small frequency compositions in the range of 100–150 Hz and at 240 Hz (Fig. 4c–e). The perturbed frequency components can be valuably exploited in future optical communications, as information can be effectively ciphered and decoded through the modulated amplitude, frequency and also the phase of the current.

Furthermore, the temporal direction switching of photoelectron injection under 60 Hz 254 nm UV is unique to the demonstrated LiCl:$FAPbCl_3$ photodetector. Through chronoamperometry studies on a commercial Si photodiode with lateral interdigitated electrodes, we found that 60 Hz 254 nm UV photons did not give rise to any bipolar photoelectron injections, as manifested by the photocurrent signals that are one-sided to the background dark currents, although the benchmark Si photodiode is also capable of sensitively detecting the AC-powered 254 nm and 365 nm UV photons *via* periodic oscillatory currents (Fig. S10 and S11†). The indifferent photoresponse of the Si photodiode under 254 nm and 365 nm irradiation implies the absence of distinguishability toward UV photons with different energies in a regular device architecture with interdigitated electrodes. Importantly, the back electron transfer under 60 Hz 254 nm UV is further validated through chronopotentiometry studies, where LiCl:$FAPbCl_3$ demonstrates bipolar photovoltage signals with respect to the background V_{oc} under 254 nm AC-powered UV illumination; meanwhile, 365 nm AC-powered UV photons lead to on–off photovoltage signals that are one-sided to the V_{oc}, as shown in Fig. S12.†

To account for the photophysical origin of bipolar photoresponses under 60 Hz 254 nm UV photons, UV-vis absorbance was subsequently performed on LiCl:$FAPbCl_3$ nanostructured pellets. As shown in Fig. S13a,† absorbance at 254 nm (1.878) and 365 nm (0.179) leads to a ratio of corresponding absorption coefficients of ~10.5 according to the Beer–Lambert equation:

$$A = \alpha c l$$

in which α, c and l stand for the absorption coefficient and density and thickness of the material, respectively. Under average optical power densities of 60 Hz 254 nm (0.007532 mW cm^{-2}) and 365 nm (0.008517 mW cm^{-2}), the difference in absorption coefficients therefore results in 254 nm photoelectrons that are 6 times greater in number over the 365 nm photoelectrons. Explicitly, the large number of 254 nm photoelectrons is manifested in the large responsivity (~1.54 A W^{-1}) and photocurrent magnitude that is nearly 4 times that of the photocurrent achieved under 365 nm AC-powered UV, as shown in Fig. S13b.† It is noteworthy that the

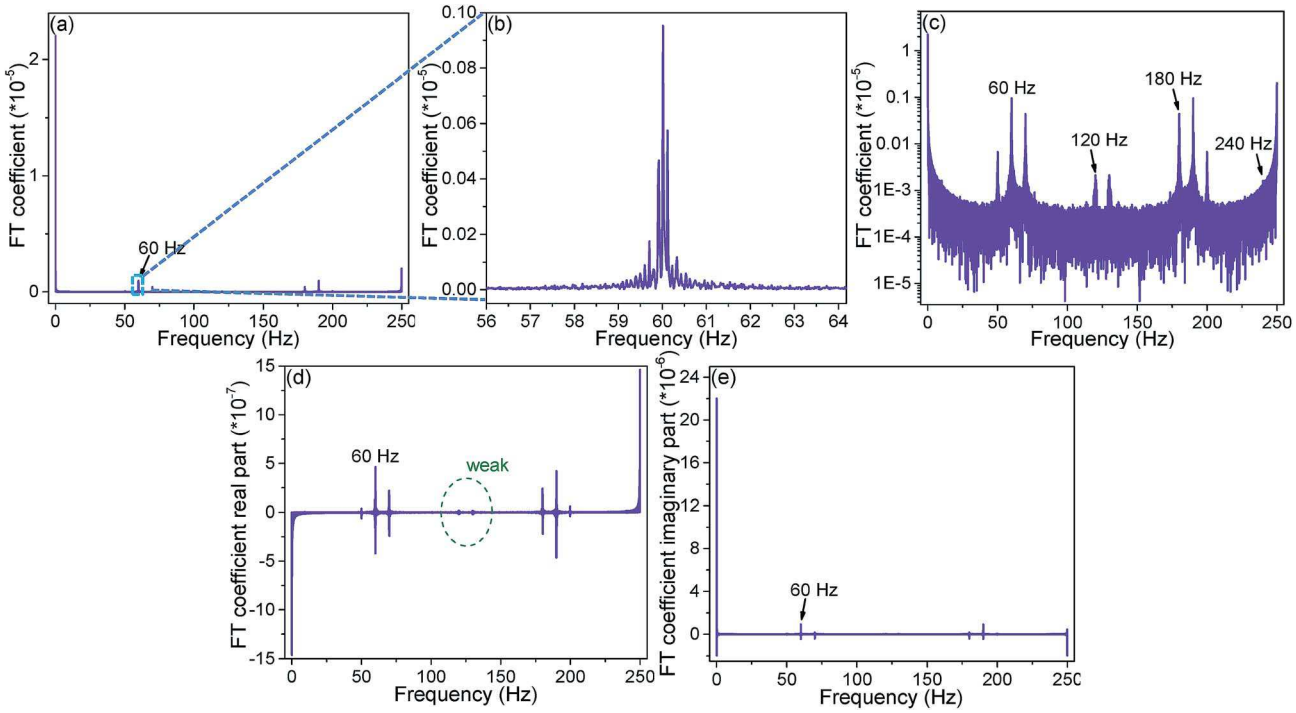

Fig. 4 FT of the chronoamperogram measured under 60 Hz 254 nm UV as shown in Fig. 3d for the LiCl:$FAPbCl_3$ nanostructured film. (a) FT coefficient plot. (b) Zoomed-in view of the coefficient plot in the range of 56 to 64 Hz. (c) Logarithmic scale of the coefficient plot. (d) and (e) real-part and imaginary-part coefficient plots, respectively.

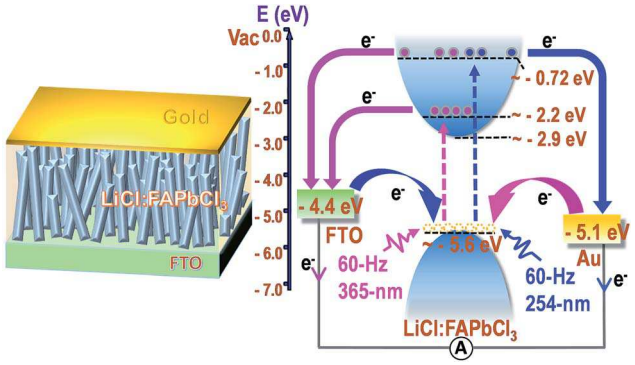

Fig. 5 Schematic illustration of the energy band diagram and migration of photoexcited electrons (right) in the FTO/LiCl:FAPbCl$_3$/Au device (left) under 365 nm and 254 nm AC-powered UV illuminations.

photocurrent densities summarized in Fig. S13b† are average magnitudes in order to be on par with the average optical power densities measured using a light meter (LI-250A), *via* the following equation due to their sinusoidally oscillating nature:

$$J_{avg} = \frac{2J_p}{\pi}$$

where J_p and J_{avg} respectively represent the peak and average photocurrent densities. Fundamentally, it is the large concentration of 254 nm-induced photocarriers in the conduction band of LiCl:FAPbCl$_3$ that enables bipolar electron injections, where electrons selectively flow toward the FTO side at the beginning of 254 nm UV illumination due to the much scarcer density of states in FTO than that in metallic gold, which can be clearly perceived from the semi-metallic nature[41,42] of FTO. After FTO is fully saturated with electrons, migration of photoelectrons will switch to the gold side, with the whole charge transfer process repeating reciprocally between the two electrodes, as illustrated in Fig. 5, where the energy levels of the valence band maximum and conduction band minimum are determined by ultraviolet photoelectron spectroscopy (Fig. S14†) and the optical bandgap (~2.7 eV, Fig. S13a†). Additionally, the absorbance spectrum of LiCl:FAPbCl$_3$ (Fig. S13a†) distinctively reveals an onset area (between 350 and 500 nm) that is smoothly followed by a drastic rise of absorbance below 350 nm, which was unforeseen in other perovskite materials[43–48] and implies exponentially increased conduction band states (greater bandwidths) at higher energy levels. The significantly greater bandwidth at higher energy in the conduction band allows accommodating more photoelectrons excited by 254 nm UV light, and thus greatly augments the probability of bipolar photoelectron injections as compared with photoelectrons excited under 365 nm UV.

Conclusions

In summary, we conducted chronoamperometry studies of a high-crystallinity LiCl:FAPbCl$_3$ nanostructured photodetector, which exhibits prominent distinguishability towards AC-powered 365/254 nm UV illuminations in the way of periodically oscillating and bipolar photoelectron injections into FTO and Au electrodes. On–off photovoltages further verify the observed current polarities in the LiCl:FAPbCl$_3$ device. Fundamentally, the photophysical origin of the observed bipolar photoresponse under AC-powered 254 nm UV illumination lies in the large number and wide conduction bandwidth of the 254 nm excited photoelectrons. From the structural perspectives, the highly ordered morphology and directional alignment of LiCl:FAPbCl$_3$ nanorods help to guide the massive number of the 254 nm excited photoelectrons towards charge collection electrodes, thereby suppressing the noise current. The demonstrated bipolar photoresponse provides an additional dimension to cipher and decipher information, in addition to the conventionally adopted amplitude and frequency modulations. Also, with different charge collection electrodes and meticulous band structure engineering, we can correspondingly tune the energy levels of photodetectors to distinguish more UV wavelengths. Our work will significantly contribute to the development of UV-based optical communications and perovskite optoelectronics with novel functionalities.

Conflicts of interest

There are no conflicts to declare.

Acknowledgements

T. X. acknowledges support from the U.S. National Science Foundation (DMR-1806152). Part of this work was performed at the Center for Nanoscale Materials, a U.S. Department of Energy Office of Science User Facility, and supported by the U.S. Department of Energy, Office of Science, under Contract No. DE-AC02-06CH11357. W. H. and T. J. M. acknowledge support from Northwestern University National Science Foundation MRSEC (DMR-1720139). Ian Zhang is a summer high school student volunteer from Naperville Neuqua Valley High School. J. G. acknowledges the experimental support from Prof. Elizabeth R. Gaillard.

Notes and references

1 M. Z. Chowdhury, M. T. Hossan, A. Islam and Y. M. Jang, *IEEE Access*, 2018, **6**, 9819–9840.
2 Z. Xu and B. M. Sadler, *IEEE Commun. Mag.*, 2008, **46**, 67–73.
3 X. Sun, Z. Zhang, A. Chaaban, T. K. Ng, C. Shen, R. Chen, J. Yan, H. Sun, X. Li, J. Wang, J. Li, M.-S. Alouini and B. S. Ooi, *Opt. Express*, 2017, **25**, 23267–23274.
4 H. Qin, Y. Zuo, D. Zhang, Y. Li and J. Wu, *Opt. Express*, 2017, **25**, 5018–5030.
5 Z. Xu, G. Chen, F. Abou-Galala and M. Leonardi, *Proc. SPIE*, 2007, **6709**, 67090Y.
6 T.-f. Zhao, A.-l. Zhang and R.-l. Xue, *Optoelectron. Lett.*, 2013, **9**, 208–212.
7 L. Dou, Y. Yang, J. You, Z. Hong, W.-H. Chang, G. Li and Y. Yang, *Nat. Commun.*, 2014, **5**, 5404.

8 M. Zhang, F. Zhang, Y. Wang, L. Zhu, Y. Hu, Z. Lou, Y. Hou and F. Teng, *Sci. Rep.*, 2018, **8**, 11157.
9 Q. Han, S.-H. Bae, P. Sun, Y.-T. Hsieh, Y. Yang, Y. S. Rim, H. Zhao, Q. Chen, W. Shi, G. Li and Y. Yang, *Adv. Mater.*, 2016, **28**, 2253–2258.
10 G. Maculan, A. D. Sheikh, A. L. Abdelhady, M. I. Saidaminov, M. A. Haque, B. Murali, E. Alarousu, O. F. Mohammed, T. Wu and O. M. Bakr, *J. Phys. Chem. Lett.*, 2015, **6**, 3781–3786.
11 W. Deng, L. Huang, X. Xu, X. Zhang, X. Jin, S.-T. Lee and J. Jie, *Nano Lett.*, 2017, **17**, 2482–2489.
12 Z. Zhang, W. Zheng, R. Lin and F. Huang, *R. Soc. Open Sci.*, 2018, **5**, 180905.
13 W. Wang, H. Xu, J. Cai, J. Zhu, C. Ni, F. Hong, Z. Fang, F. Xu, S. Cui, R. Xu, L. Wang, F. Xu and J. Huang, *Opt. Express*, 2016, **24**, 8411–8419.
14 J. Zhang, Q. Wang, X. Zhang, J. Jiang, Z. Gao, Z. Jin and S. Liu, *RSC Adv.*, 2017, **7**, 36722–36727.
15 S. Govinda, B. P. Kore, D. Swain, A. Hossain, C. De, T. N. G. Row and D. D. Sarma, *J. Phys. Chem. C*, 2018, **122**, 13758–13766.
16 Y. Yang, Y. Jin, H. He, Q. Wang, Y. Tu, H. Lu and Z. Ye, *J. Am. Chem. Soc.*, 2010, **132**, 13381–13394.
17 J. T. Wang, X. L. Shi, W. W. Liu, X. H. Zhong, J. N. Wang, L. Pyrah, K. D. Sanderson, P. M. Ramsey, M. Hirata and K. Tsuri, *Sci. Rep.*, 2014, **4**, 3679.
18 C. Zhou, Y. Tian, O. Khabou, M. Worku, Y. Zhou, J. Hurley, H. Lin and B. Ma, *ACS Appl. Mater. Interfaces*, 2017, **9**, 40446–40451.
19 G. Liu, J. Gong, L. Kong, R. D. Schaller, Q. Hu, Z. Liu, S. Yan, W. Yang, C. C. Stoumpos, M. G. Kanatzidis, H.-k. Mao and T. Xu, *Proc. Natl. Acad. Sci. U. S. A.*, 2018, **115**, 8076–8081.
20 M. Soleymani and M. Edrissi, *Bull. Mater. Sci.*, 2016, **39**, 487–490.
21 L. Zaraska, K. Mika, K. E. Hnida, M. Gajewska, T. Lojewski, M. Jaskula and G. D. Sulka, *Mater. Sci. Eng., B*, 2017, **226**, 94–98.
22 R.-G. Ciocarlan, E. M. Seftel, M. Mertens, A. Pui, M. Mazaj, N. N. Tusar and P. Cool, *Mater. Sci. Eng., B*, 2018, **230**, 1–7.
23 N. J. Jeon, J. H. Noh, W. S. Yang, Y. C. Kim, S. Ryu, J. Seo and S. I. Seok, *Nature*, 2015, **517**, 476–480.
24 M. I. Saidaminov, A. L. Abdelhady, G. Maculan and O. M. Bakr, *Chem. Commun.*, 2015, **51**, 17658–17661.
25 T. M. Koh, K. Fu, Y. Fang, S. Chen, T. C. Sum, N. Mathews, S. G. Mhaisalkar, P. P. Boix and T. Baikie, *J. Phys. Chem. C*, 2014, **118**, 16458–16462.
26 M. Yang, T. Zhang, P. Schulz, Z. Li, G. Li, D. H. Kim, N. Guo, J. J. Berry, K. Zhu and Y. Zhao, *Nat. Commun.*, 2016, **7**, 12305.
27 X. Cao, L. Zhi, Y. Li, F. Fang, X. Cui, L. Ci, K. Ding and J. Wei, *ACS Appl. Energy Mater.*, 2018, **1**, 868–875.
28 Y. Fu, F. Meng, M. B. Rowley, B. J. Thompson, M. J. Shearer, D. Ma, R. J. Hamers, J. C. Wright and S. Jin, *J. Am. Chem. Soc.*, 2015, **137**, 5810–5818.
29 H. Zhu, Y. Fu, F. Meng, X. Wu, Z. Gong, Q. Ding, M. V. Gustafsson, M. T. Trinh, S. Jin and X.-Y. Zhu, *Nat. Mater.*, 2015, **14**, 636–642.
30 T. Bu, X. Liu, Y. Zhou, J. Yi, X. Huang, L. Luo, J. Xiao, Z. Ku, Y. Peng, F. Huang, Y.-B. Cheng and J. Zhong, *Energy Environ. Sci.*, 2017, **10**, 2509–2515.
31 X. Liu, Y. Zhang, L. Shi, Z. Liu, J. Huang, J. S. Yun, Y. Zeng, A. Pu, K. Sun, Z. Hameiri, J. A. Stride, J. Seidel, M. A. Green and X. Hao, *Adv. Energy Mater.*, 2018, **8**, 1800138.
32 J. H. Jun, H. Seong, K. Cho, B.-M. Moon and S. Kim, *Ceram. Int.*, 2009, **35**, 2797–2801.
33 E.-J. Guo, J. Xing, K.-J. Jin, H.-B. Lu, J. Wen and G.-Z. Yang, *J. Appl. Phys.*, 2009, **106**, 023114.
34 E.-J. Guo, J. Xing, H.-B. Lu, K.-J. Jin, J. Wen and G.-Z. Yang, *J. Phys. D: Appl. Phys.*, 2009, **43**, 1.
35 J. Xing, E. Guo, K.-j. Jin, H. Lu, J. Wen and G. Yang, *Opt. Lett.*, 2009, **34**, 1675–1677.
36 Y. C. Kim, K. H. Kim, D.-Y. Son, D.-N. Jeong, J.-Y. Seo, Y. S. Choi, I. T. Han, S. Y. Lee and N.-G. Park, *Nature*, 2017, **550**, 87–91.
37 H. Wang, J. Huang, S. Xing and J. Yu, *Org. Electron.*, 2016, **28**, 11–19.
38 G. Hodes, *J. Phys. Chem. Lett.*, 2015, **6**, 4090–4092.
39 C. Yang, Z. Wang, T. Lin, H. Yin, X. Lu, D. Wan, T. Xu, C. Zheng, J. Lin, F. Huang, X. Xie and M. Jiang, *J. Am. Chem. Soc.*, 2013, **135**, 17831–17838.
40 M. G. Walter, E. L. Warren, J. R. McKone, S. W. Boettcher, Q. Mi, E. A. Santori and N. S. Lewis, *Chem. Rev.*, 2010, **110**, 6446–6473.
41 Z. Yang, S. Gao, T. Li, F.-Q. Liu, Y. Ren and T. Xu, *ACS Appl. Mater. Interfaces*, 2012, **4**, 4419–4427.
42 M. Turrion, B. Macht, H. Tributsch and P. Salvador, *J. Phys. Chem. B*, 2001, **105**, 9732–9738.
43 L. Kong, G. Liu, J. Gong, Q. Hu, R. D. Schaller, P. Dera, D. Zhang, Z. Liu, W. Yang, K. Zhu, Y. Tang, C. Wang, S.-H. Wei, T. Xu and H.-k. Mao, *Proc. Natl. Acad. Sci. U. S. A.*, 2016, **113**, 8910–8915.
44 Y. Zhou, M. Yang, W. Wu, A. L. Vasiliev, K. Zhu and N. P. Padture, *J. Mater. Chem. A*, 2015, **3**, 8178–8184.
45 W. Ke, G. Fang, J. Wan, H. Tao, Q. Liu, L. Xiong, P. Qin, J. Wang, H. Lei, G. Yang, M. Qin, X. Zhao and Y. Yan, *Nat. Commun.*, 2015, **6**, 6700.
46 T. M. Koh, V. Shanmugam, X. Guo, S. S. Lim, O. Filonik, E. M. Herzig, P. Müller-Buschbaum, V. Swamy, S. T. Chien, S. G. Mhaisalkar and N. Mathews, *J. Mater. Chem. A*, 2018, **6**, 2122–2128.
47 J. Chen, X. Lian, Y. Zhang, W. Yang, J. Li, M. Qin, X. Lu, G. Wu and H. Chen, *J. Mater. Chem. A*, 2018, **6**, 18010–18017.
48 M. Wang, B. Li, P. Siffalovic, L.-C. Chen, G. Cao and J. Tian, *J. Mater. Chem. A*, 2018, **6**, 15386–15394.